

Size distribution of small grains in the inner zodiacal cloud

J. R. SZALAY ¹, P. POKORNÝ ^{2,3} AND D. M. MALASPINA ^{4,5}¹*Department of Astrophysical Sciences, Princeton University, 171 Broadmead St., Princeton, NJ 08540, USA*²*Astrophysics Science Divison, NASA Goddard Spaceflight Center, Greenbelt, MD, 20771, USA*³*Department of Physics, The Catholic University of America, Washington, DC, 20064, USA*⁴*Department of Astrophysical and Planetary Sciences, University of Colorado Boulder, Boulder, CO, USA*⁵*Laboratory for Atmospheric and Space Physics, University of Colorado Boulder, Boulder, CO, USA*

Submitted to PSJ

ABSTRACT

The Parker Solar Probe (PSP) spacecraft has transited the inner-most regions of the zodiacal cloud and detects impacts to the spacecraft body via its electric field instrument. Multiple dust populations have been proposed to explain the PSP dust impact rates. PSP’s unique orbit allows us to identify a region where the impact rates are likely dominated by α -meteoroids, small zodiacal grains on approximately circular, bound orbits. From the distribution of voltage signals generated by dust impacts to PSP in this region, we find the cumulative mass index for grains with radii of $\sim 0.6\text{--}1.4\ \mu\text{m}$ (masses of 3×10^{-15} to 3×10^{-14} kg) to be $\alpha = 1.1 \pm 0.3$ from $0.1\text{--}0.25\ R_{\odot}$. α increases toward the Sun, with even smaller fragments generated closer to the Sun. The derived size distribution is steeper than previously estimated, and in contrast to expectations we find most of the dust mass resides in the smallest fragments and not in large grains inside $0.15\ \text{au}$. As the inner-most regions of the zodiacal cloud are likely collisionally evolved, these results place new constraints how the solar system’s zodiacal cloud and by extension astrophysical debris disks are partitioned in mass.

1. INTRODUCTION

Our solar system’s zodiacal cloud comprises multiple dust populations. Of the interplanetary populations, these are typically categorized as α -meteoroids¹: gravitationally bound grains on elliptic trajectories and β -meteoroids: grains so small the outward force of solar radiation overcomes the inward pull of the Sun’s gravity such that they are pushed out of the solar system on hyperbolic trajectories (Zook & Berg 1975; Wehry & Mann 1999). These dust populations are continuously evolving and exchanging material due to dynamical evolution from gravity, solar radiation, and electromagnetic forces, as well as disruption from collisions, sublimation,

and rotation (Mann et al. 2004). This cloud also provides an important analog to study exozodiacal systems.

A key quantity that directly affects β -meteoroid production and zodiacal erosion is how collisional fragment particles are distributed in mass, which has not been well constrained near the Sun. Collisional products are often assumed to follow a power-law mass distribution (e.g. Gault & Wedekind 1969; Dohnanyi 1969), such that the immediate fragmented differential mass distribution is $f(m) \propto m^{-(\eta+1)}$. These collisional products can then undergo mass-dependent transport and erosion, such that the instantaneous differential mass distribution at any location in the heliosphere has the form

$$f(m) \propto m^{-(\alpha+1)} \quad (1)$$

where α is the cumulative mass index. In this study, we assume the cumulative fragmentation index η and the cumulative mass index α are equal, such $\eta = \alpha$. Note, α as the variable used to represent mass index does not have any relation to the term ‘ α -meteoroid’, where we use ‘ α ’ in both cases for historical consistency. Changes in α directly affect how much material the zodiacal cloud

Corresponding author: Jamey Szalay
jszalay@princeton.edu

¹ There are two definitions of α -meteoroids in the literature (Sommer 2023): 1) a dynamical subset of gravitationally bound grains with very large eccentricities and 2) all grains gravitationally bound to the Sun. We use the latter, broad definition for α -meteoroids.

retains or sheds through its production of β -meteoroids. Hence, an accurate determination of α reveals the effect of collisional fragmentation on zodiacal evolution.

There have been a number of both observational and ground-based experimental constraints on α . Ground-based collision experiments found values of $\alpha = 0.5 - 1.0$ for collisionally generated material (e.g. Krivov et al. 2000, and refs. therein). The size distribution of lunar ejecta in the radius range of $0.3 - 10 \mu\text{m}$ was consistent with $\alpha = 0.9$ (Horányi et al. 2015), while initial Solar Orbiter (SolO) results (Zaslavsky et al. 2021) found values of $\alpha = 0.3 - 0.4$ for β -meteoroids with radii of $\sim 100\text{-}200 \mu\text{m}$. The zodiacal cloud in the outer solar system beyond Saturn’s orbit as measured by New Horizons’ Student Dust Counter observations (Piquette et al. 2019) was found to be consistent with $\alpha = 0.5 - 1.2$ by comparing with a dynamical model of the outer zodiacal grain distribution (Poppe 2016). More recent collisional modeling in the inner solar system concluded $\alpha = 1.11 \pm 0.03$ for grains with radii $> 100 \mu\text{m}$ (Pokorný et al. 2024). From modeling the near-Sun zodiacal cloud, $\alpha = 0.5 - 0.6$ was expected at a heliocentric distance of 0.1 au for micron-sized grains (Ishimoto & Mann 1998).

While unequipped with a dedicated dust detector, Parker Solar Probe (PSP) spacecraft (Fox et al. 2016) registers dust impacts primarily via voltage measurements with the FIELDS instrument (Bale et al. 2016). There has been an extensive history of measuring dust impacts from spacecraft equipped with electric field instruments, for example: Voyager 2 (Gurnett et al. 1983), Vega (Laakso et al. 1989), DS-1 (Tsurutani et al. 2003; Tsurutani et al. 2004), Wind (Malaspina et al. 2014; Kellogg et al. 2016; Malaspina et al. 2016), MAVEN (Andersson et al. 2015), Cassini (Ye et al. 2014), STEREO (Zaslavsky et al. 2012; Malaspina et al. 2015) and MMS (Vaverka et al. 2018, 2019).

During its first three orbits, impact rates observed by PSP were consistent with fluxes of dominantly high-speed, submicron-sized β -meteoroids leaving the solar system on escaping orbits (Szalay et al. 2020; Page et al. 2020; Malaspina et al. 2020). Grains smaller than β -meteoroids, often termed nanograins, are less susceptible to radiation pressure and their dynamics are dominated by electromagnetic forces; these nanograins were not found to be dominantly responsible for the impact rates during PSP’s 2nd orbit (Mann & Czechowski 2020). A two-component model consisting of both α -meteoroids and β -meteoroids was subsequently used to explain the first six orbits of impact rate data (Szalay et al. 2021), which was able to well-reproduce the majority of the impact rates observed. Additionally, a PSP dust database has been published which is continually

updated as more data is taken throughout the PSP mission (Malaspina et al. 2023).

In this study, we will calculate the cumulative impact amplitude distributions for all PSP-derived dust impact rates (Malaspina et al. 2023). Comparing to the existing two-component model, we identify a region in a subset of PSP orbits dominated by α -meteoroids in the heliocentric distance range of $0.1 - 0.25 \text{ au}$ and fit the impact amplitude distributions to a power-law. This will allow us to quantitatively constrain the size distribution of small, bound α -meteoroids in the near-Sun environment.

2. PSP DUST IMPACT RATES FROM ORBITS 1-17

Figure 1 shows the dust impact rates (Malaspina et al. 2023) to PSP as a function of position and time from orbits 1-17. There are six orbital groupings for the spacecraft shown: 1-3, 4-5, 6-7, 8-9, 10-16, & 17. There are a few notable features in the impact rates: all orbits exhibit a peak pre-perihelion, with lower impact rates observed at perihelion, followed often by a post-perihelion peak that is lower in total rate than the pre-perihelion peak. A two-component model consisting of prograde α -meteoroids and β -meteoroids was used to successfully model PSP impact rates from orbits 1-6 (Szalay et al. 2021). Note, this model incorporates the updated density profile of the zodiacal cloud derived from PSP imaging (Stenborg et al. 2020). Figure 2a shows an example of this two-component model fit to the impact rates from orbit 13 as a representative example. The model predicts a symmetric pre- and post-perihelion impact rate peak from the α -meteoroid population (green line) and an asymmetric profile for the β -meteoroid population. Due to the spacecraft velocity addition with the solely outbound, prograde β -meteoroids, the impact rate from β -meteoroids is expected to exhibit a strong pre-perihelion peak and significantly depleted impact rates just after perihelion due to PSP “catching up” to the β -meteoroids and having much smaller relative impact speeds and corresponding impact rates.

The two-component model successfully fits the majority of impact rate structure observed by PSP, with the exception of the post-perihelion peak magnitude for orbits 4-5. During these orbits, which exhibited a post-perihelion impact rate peak that could not be explained by the two-component model, it was proposed that a third component of collisionally produced β -meteoroids from the Geminids stream, termed a β -stream, could be responsible for the additional enhancement (Szalay et al. 2021). It was shown that PSP would have intersected the trajectories of β -meteoroids produced during collisions between the Geminids and zodiacal cloud in orbits

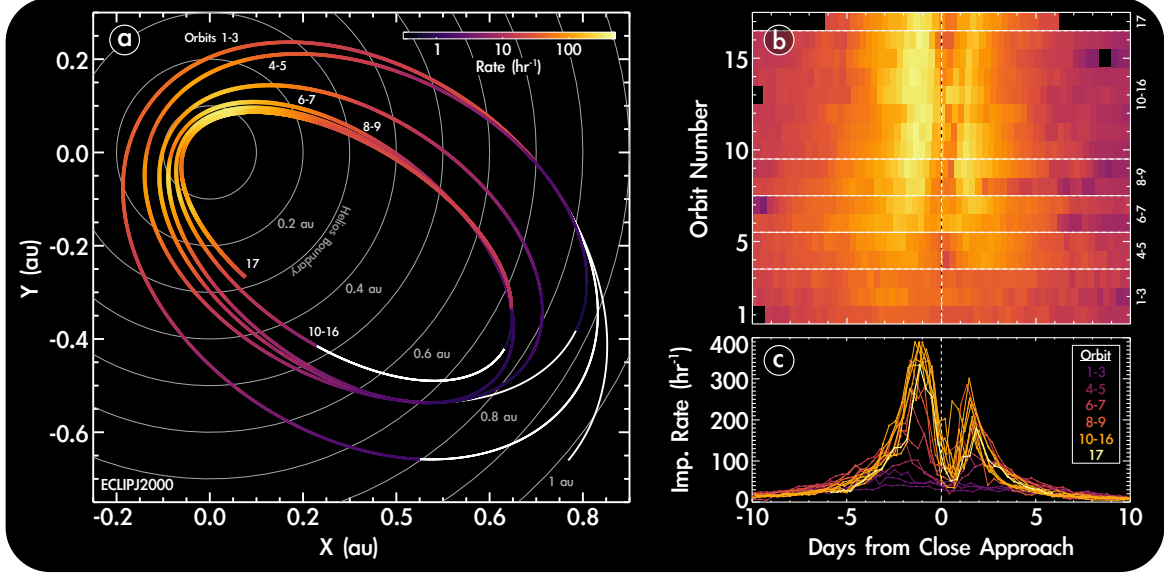


Figure 1. Impact rates for PSP’s first 17 orbits. (a) Top-down view in Ecliptic J2000 coordinates, where rates within each orbital group are averaged. The inner-most location of the Helios dust measurements (Grün et al. 1980) outside 0.3 au is also indicated. (b, c) Time-series of each orbit, where the colorbar in (b) is shared with that of (a), as a function days from perihelion.

4-5. Subsequent directional analysis was also supportive of a β -stream hypothesis (Pusack et al. 2021). Modeling efforts on the overall Geminids stream found the bound α -meteoroids within the Geminids could not be responsible for the additional rate enhancement (Cukier & Szalay 2023), indirectly supporting the β -stream hypothesis. However, without dedicated dust instrumentation it is difficult to definitively conclude the origins of the post-perihelion enhancement during orbits 4-5.

Aside from orbits 4-5, the model is able to well-reproduce the magnitude and location of the post-perihelion enhancement. This region, just after perihelion, is the primary focus of this study as it is expected to be dominated by impacts from α -meteoroids, with minimal contributions from β -meteoroids. Figures 2b & c show the impact fraction of α -meteoroids (green) and β -meteoroids (purple) throughout orbit 13. As shown here, the region just after perihelion to ~ 5 days post-perihelion has less than a few percent contribution from β -meteoroids. Therefore, due to PSP’s highly eccentric orbit, this region provides a unique opportunity to isolate the α -meteoroid population and analyze its properties. We focus on this region throughout the remainder of this study and derive the size distribution power-law index for α -meteoroids here. Additionally, we focus on orbits 10-16 as they provide seven nearly identical trajectories to sample this region and provide a statistical dataset with which to study α -meteoroids in the near-Sun zodiacal cloud.

3. DETERMINING THE SIZE DISTRIBUTION

Here, we outline a method to derive the cumulative mass index α from the distribution of impact voltages to PSP. Dust impacts are measured by PSP as a potential change $\Delta V \propto Q_{\text{imp}}$ (Collette et al. 2014; Shen et al. 2023). In order to relate the impact charge distribution to the impact mass distribution, we assume the differential charge distribution has the form $f(Q) \propto Q^{-(\alpha_Q+1)}$, where α_Q is the cumulative charge index. In the Appendix, we derive a relation between α_Q and α that allows us to estimate the mass index from the distribution of measured impact voltages as similarly done for radar observations of meteors with a speed-dependent radar amplitude (Pokorný & Brown 2016).

To ensure PSP is being impacted by a single population, we focus on times where the spacecraft resides between 0.1 to 0.25 au ($22\text{-}54 R_\odot$) post-perihelion, as the two-component model predicts α -meteoroids contribute $>95\%$ of the total impacts throughout this region for orbits 10-16. We note interstellar grains could also be impacting PSP in this region (Sterken et al. 2012; Strub et al. 2019), where due to PSP’s orbit geometry these grains would be most readily detected during the post-perihelion arc far from the Sun. However, given the ability of the two-component model to reasonably reproduce the location and amplitude of the second peak during orbits 10-16 and that much of the interstellar dust grains are dynamically prevented from transiting very near to the Sun due to radiation pressure, we do not expect this source to appreciably contribute to PSP’s impact rates in this region.

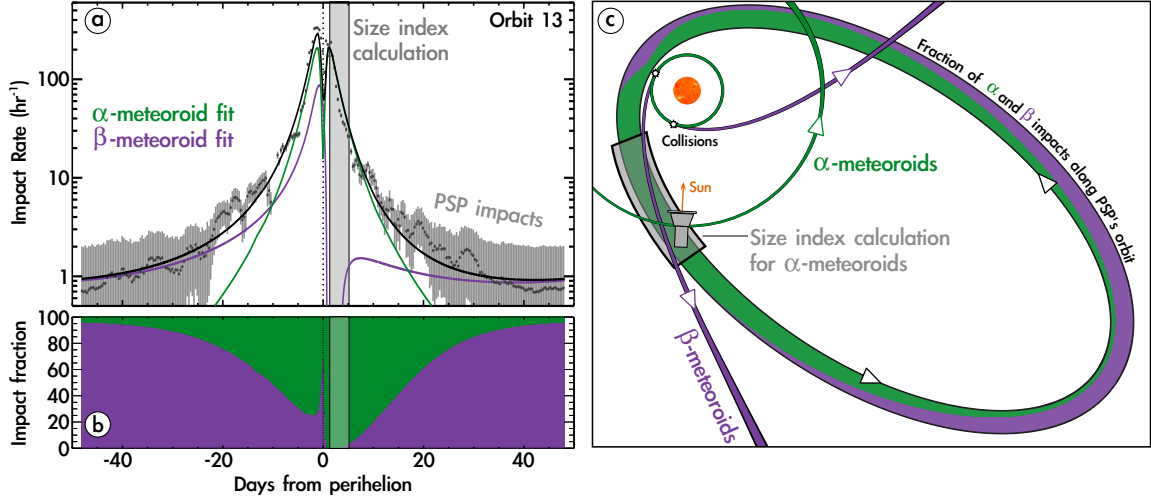


Figure 2. (a) Example impact rate from orbit 13, representative of orbits 10-16, along with the modeled abundances of α -meteoroids and β -meteoroids from our two-component fit (Szalay et al. 2021). (b) Fractional contribution of α -meteoroids and β -meteoroids to total modeled impact rate. (c) Same information as panel (b) shown in the ecliptic J2000 x-y plane with example α -meteoroid & β -meteoroid trajectories.

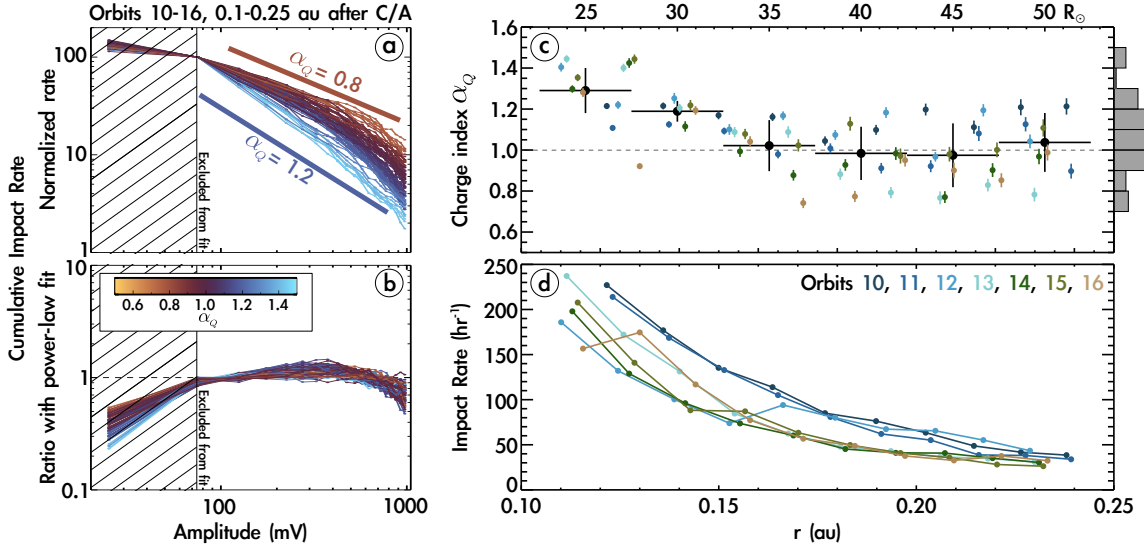


Figure 3. (a) Cumulative impact rate distribution as a function of impact amplitude for orbits 10-16, with color indicating the power-law fit index above 50 mV for each 8-hr impact rate interval considered. (b) Ratio of cumulative impact rates with their corresponding power-law fits. (c) Cumulative charge indices α_Q as a function of heliocentric distance, with average values and standard deviation each 5 R_\odot and the histogram on the right shows the distribution of α_Q values. (d) Impact rates as a function of heliocentric distance. Colors for (c) & (d) show orbit number

Figure 3a shows the ensemble of cumulative impact-amplitude distributions measured by PSP for each 8-hour segment within the selected portions of orbits 10-16. Each voltage range is displayed at the center of a 50 mV bin, such that the first voltage point in the shaded region corresponds to 0-50 mV, the second point to 50-100 mV, and so forth. Due to the dust impact identification method, impacts with amplitudes below 50 mV (the first point in each curve) are more challeng-

ing to detect (Malaspina et al. 2023) and we are likely not identifying all impacts below this amplitude, hence the break in the slope of the distribution at this amplitude as shown in Figure 3a. Additionally, this measurement technique saturates above 950 mV, therefore we can probe the size-distribution index within a single decade in mass. We fit the cumulative amplitude distribution above 50 mV to a power-law, where the colors of the various curves in Figure 3a shows the cumulative

charge index α_Q . Figure 3b shows these same cumulative impact rate curves divided by their corresponding power-law fits. As shown here, the cumulative voltage distributions are highly consistent with power-laws. In Figure 3c, we show the fitted charge indices as a function of heliocentric distance, along with average values in 5 R_\odot bins. Figure 3d shows the total impact rates for each orbit, where Figures 3c & d are colored by orbit number.

We previously estimated the minimum detectable bound α -meteoroid grain radius to be approximately 0.6 μm for a threshold of 50 mV (Szalay et al. 2021). With the additional uncertainty discussed in the Appendix, this lower limit could be down to ~ 0.5 μm , however, grains as small as 0.5 μm in radius are expected to have $\beta \approx 0.5$ and would be unbound. Therefore, we retain our lower limit estimate to be 0.6 μm . As the PSP impact voltages used here have a dynamic range of 50–950 mV, we are able to assess the mass distribution within a decade in mass from the minimum detectable size such that the derived indices are relevant for grains with radii of approximately 0.6 – 1.4 μm .

As derived in the Appendix, $\alpha = \alpha_Q(1 + \delta a)$ relates the cumulative charge index α_Q to the cumulative mass index α . Figure 4a shows δa as a function of heliocentric distance, where this term is most enhanced for closer heliocentric distances. We use these δa ranges to correct the derived cumulative charge indices α_Q from Figure 3c. Considering both the upper and lower limits of δa , Figures 4b & 4c show the range of corrected mass indices. For each 5 R_\odot heliocentric bin, we determine the full range of possible α values from these two panels and display it in panel (d) with the average value of these ranges shown with black circles. The grey circles overlaid on these show the uncorrected ranges of α_Q from Figure 3c. While this mass-dependent correction is important to consider, we find it does not have a substantial effect on the dependence of α on α_Q .

The mass indices shown in Figure 3d, represent our best estimate of α correcting for mass-dependent biases discussed. Throughout this region, from the full uncertainty ranges in Figure 3d, we find $\alpha = 1.1 \pm 0.3$. Additionally, we find the mass index is higher near the Sun, exhibiting an enhancement in α inside ~ 0.15 au systematically above 1.0.

4. IMPLICATIONS FOR COLLISIONAL PRODUCTION

Having found $\alpha = 1.1 \pm 0.3$ in the 0.1–0.25 au range, we now focus on the implications of these mass indices in the near-Sun zodiacal dust cloud. For a collisionally produced population, the mass index determines the

maximum size grain that can be produced as a fragment. We investigate how mass is distributed, including the maximum fragment size, as a function of α . For an upper size cutoff m_c for fragments, we normalize the distribution such that the total number of particles with mass greater than or equal to m_c is 1. Therefore, the differential distribution function is

$$f(m) = \frac{\alpha}{m_c^{-\alpha} - m_1^{-\alpha}} m^{-(\alpha+1)} \quad (2)$$

where the number of particles between m_a and m_b is given by

$$N = \int_{m_a}^{m_b} f(m) dm = \frac{m_a^{-\alpha} - m_b^{-\alpha}}{m_c^{-\alpha} - m_1^{-\alpha}} \quad (3)$$

For a parent particle of mass m_1 , whose minimum fragment mass is m_0 , its collisional fragments must have a total mass of m_1 , hence,

$$m_1 = \int_{m_0}^{m_1} m f(m) dm = \frac{\alpha}{m_c^{-\alpha} - m_1^{-\alpha}} \int_{m_0}^{m_1} m^{-\alpha} dm \quad (4)$$

Therefore, the mass of the largest fragment m_c is given by

$$m_c = \begin{cases} \left(\frac{(\alpha-1)m_1}{\alpha m_0^{1-\alpha} - m_1^{1-\alpha}} \right)^{\frac{1}{\alpha}} & \text{if } \alpha \neq 1, \\ \frac{m_1}{1 + \ln(m_1/m_0)} & \text{if } \alpha = 1 \end{cases} \quad (5)$$

For a more intuitive interpretation, these relations can be approximated by assuming $m_0 \ll m_1$ and expanding to zeroth order in m_0/m_1 when $\alpha \neq 1$,

$$m_c \approx \begin{cases} m_0 \left(\frac{\alpha-1}{\alpha} \frac{m_1}{m_0} \right)^{\frac{1}{\alpha}} & \text{if } \alpha > 1, \\ m_1 (1 - \alpha)^{\frac{1}{\alpha}} & \text{if } \alpha < 1 \end{cases} \quad (6)$$

As shown in Equations 5 and 6, for $\alpha > 1$ the maximum fragment cutoff mass is most strongly governed by m_0 and weakly depends on the ratio m_1/m_0 , while for $\alpha \leq 1$ this cutoff mass is entirely governed by the original grain size m_1 . For $\alpha = 1$ it is an intermediate case mostly governed by m_1 and weakly depending on m_1/m_0 . This also means for steeper distributions with $\alpha > 1$, most of the material is in small grains near the lower end of the mass range, while shallower distributions with $\alpha \leq 1$ have most of the material in large grains toward the upper end of the mass range. Figure 5 shows a visualization of these two regimes.

Figure 6 provides a visualization of these relations. It shows the maximum fragment size r_c corresponding to grains with mass m_c as a function of assumed smallest fragment size r_0 from 10 nm to 0.3 μm corresponding to mass m_0 for different values of α . To determine radius

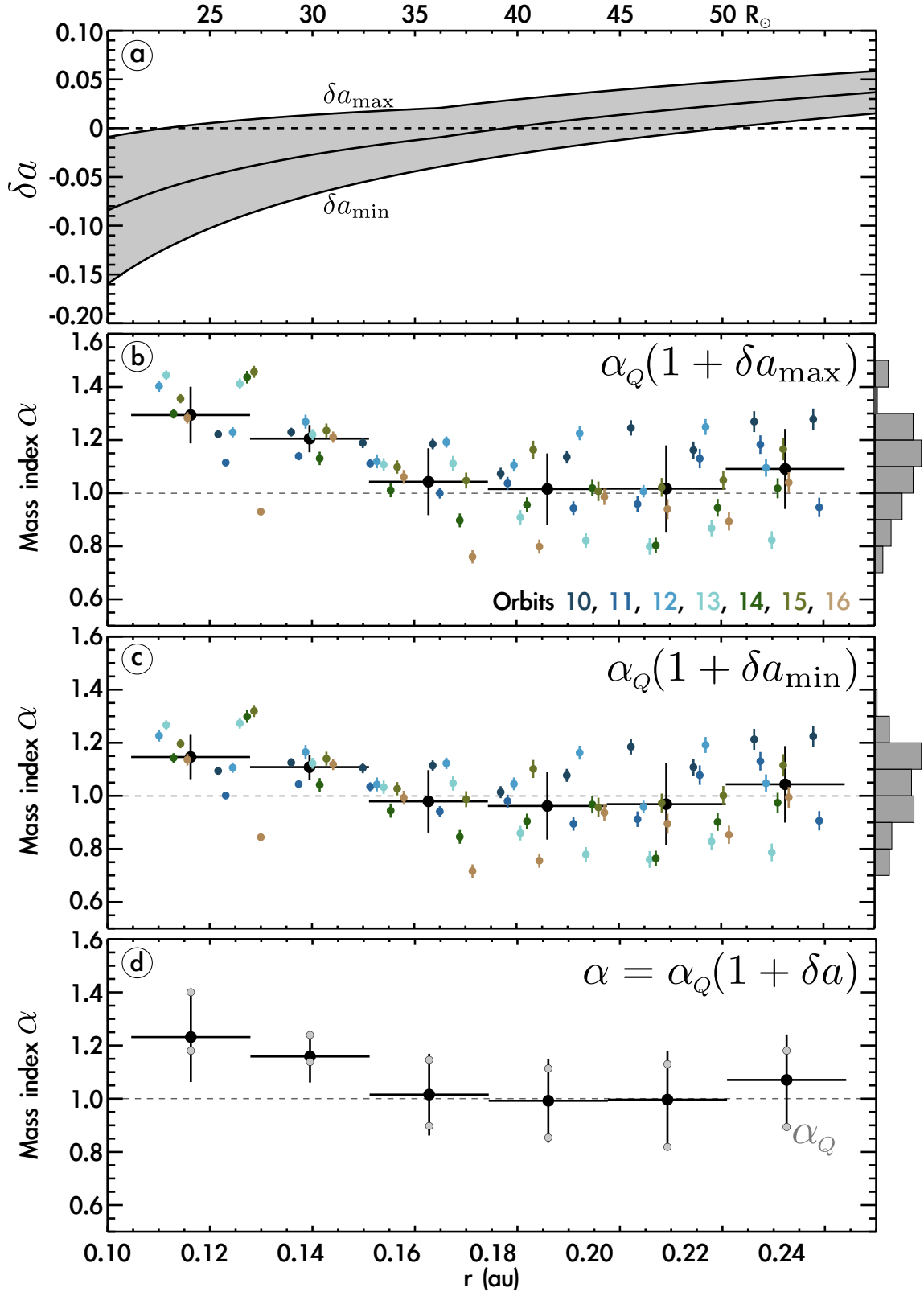


Figure 4. (a) Correction factor δa for the mass-dependent portion of the impact speed. (b) & (c) Corrected cumulative mass indices $\alpha = \alpha_Q(1 + \delta a)$ corresponding to the minimum and maximum δa values from (a). (d) Comprehensive estimate of α accounting for mass-dependent biases, with the uncorrected α_Q ranges shown with grey dots.

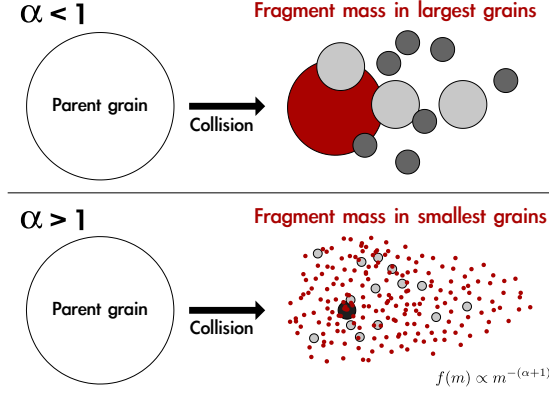


Figure 5. Distribution of fragmentation products depending on the cumulative mass index. Fragments with $\alpha > 1$ have most of the mass distributed into small grains, while for $\alpha < 1$ the majority of mass is distributed into the few largest fragments.

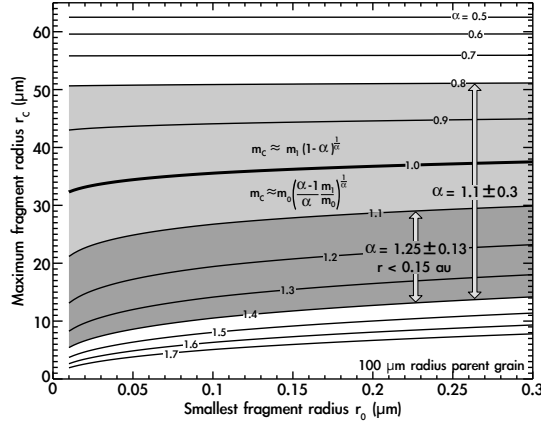


Figure 6. Maximum fragment cutoff size as a function of minimum fragment size and cumulative mass index α . The shaded region shows the average cumulative mass indices found to be consistent with the near-Sun environment.

for a given mass, we assume grains are “old cometary” origin according to Wilck & Mann (1996), with grain mass densities in the range of $2.0\text{--}3.3 \text{ g cc}^{-1}$ for grain radii of 10 nm to $20 \text{ }\mu\text{m}$. For $\alpha < 1.0$, the dependence of maximum fragment size on r_0 is weak, as most of the mass is partitioned amongst the largest grains. For $\alpha > 1.0$, most of the mass is partitioned to the smallest grains, therefore the smallest fragment size plays a larger role on determining the maximum fragment size. For the mean value of $\alpha = 1.1$, $r_c = 21$ to $30 \text{ }\mu\text{m}$ for $r_0 = 10 \text{ nm}$ to $0.3 \text{ }\mu\text{m}$ respectively. While we cannot empirically constrain r_0 in this setup, we investigate a lower limit much smaller than that of β -meteoroids. The derived mass-indices in this study, calculated from the slope of the measured voltage distributions, is insensitive to the choice of r_0 . Hence, we include the discussion of r_0 for

intuitive context and visualization of the consequences of different values of the mass index.

To provide an intuitive understanding of how these mass indices affect the near-Sun dust distribution, we visualize the size distribution of collisionally produced grains with $r_0 = 50 \text{ nm}$ and $r_1 = 100 \text{ }\mu\text{m}$ in Figure 7. This value of r_1 is chosen due to the fact that at 1 au , the majority of mass in the zodiacal cloud was found to be in $\sim 100 \text{ }\mu\text{m}$ radius grains (Grün et al. 1985), hence this size grain is likely to be the parent of much of the zodiacal collisional products. Figure 7 shows the size distribution for $\alpha = 0.6 - 2.0$ with these assumptions.

While the slopes of the different values of α are shown in the left portion of this figure, the schematic on the right visualizes how mass is distributed into collisional fragments. As previously discussed, most of the mass for $\alpha < 1.0$ is distributed into large grains and therefore collisional products in this regime have a few “large” collisional products that carry the majority of the fragmented material. However, in the regime for $\alpha > 1.0$, as found for the near-Sun environment, most of the mass gets partitioned into very small grains, while still allowing for a few larger grain fragments. With the exception of the few largest grains, the overwhelming majority of collisional mass is partitioned into the very lowest end near m_0 , which for these size ranges would all become β -meteoroids to be ejected from the solar system.

To compare to expectations, Figure 8a shows the cumulative flux of meteoroids $F(m)$ with masses $> m$ at 1 au (Grün et al. 1985). The cumulative mass index of this distribution can be calculated assuming for sufficiently small ranges in mass that the cumulative mass distribution $F(m) \propto m^{-\alpha}$, such that

$$\alpha = -\frac{m}{F(m)} \frac{dF(m)}{dm} \quad (7)$$

and shown in Figure 8b. Figure 8b shows our derived mass indices for meteoroids from 0.1 to 0.25 au of $\alpha = 1.1 \pm 0.3$ with the approximate mass/size range detectable by PSP denoted by the width of the grey rectangle. The corresponding mass index at 1 au is $\alpha = 0.35 - 0.4$ (Grün et al. 1985), therefore the mass index very near the Sun is significantly larger than its corresponding 1 au value. We also show the modeled expectation of the zodiacal flux and mass index at 0.1 au (Ishimoto & Mann 1998) with the dashed lines in Figure 8, where within the size range PSP can probe, the expected size indices at 0.1 au were expected to be $\alpha = 0.5 - 0.6$.

Both the previous expected mass indices at 0.1 and 1.0 au were below $\alpha = 1$, therefore, they were both in the regime in which most of the collisional products

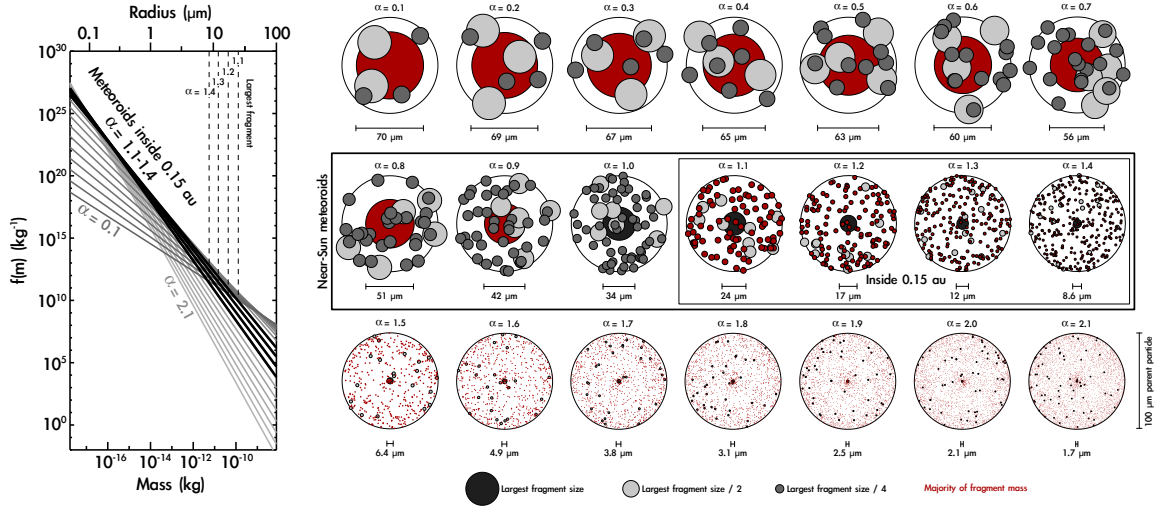


Figure 7. Size distribution of collisional fragments. (left) Differential mass distributions, with $\alpha = 1.1 \pm 0.3$ highlighted in black and the largest fragment size marked with the vertical dashed lines. (right) Visual representation of fragments, with the single largest fragment in the center and the size of the largest size fragment denoted below each. The fragments that are 1/2 and 1/4 of the largest fragment size are shown in shades of grey, with the number of circles proportional their size distribution. Red indicates where the majority of fragment mass resides, where the largest grains carry the mass for $\alpha < 1$ and smallest grains carry the mass for $\alpha > 1$.

were still large grains that would remain bound. This is in contrast to the values found here of $\alpha = 1.3 \pm 0.2$ inside 0.15 au, where effectively all collisional products immediately become β -meteoroids to be expelled from the solar system. This discrepancy may be due to the particularly intense and high speed impact environment near the Sun.

A similar technique was applied to analyze the distribution of dust impacts to SoLo (Zaslavsky et al. 2021), which found values of $\alpha = 0.3 - 0.4$. However, the index derived from SoLo impacts was likely for unbound β -meteoroids with radii of ~ 100 -200 nm, compared to the index calculated here for bound α -meteoroids of radii ~ 0.6 -1.4 μm . Additionally, the mass index derived from SoLo observations was quoted as a lower bound that may be sensitive to the distribution of β -meteoroid impact speeds which could have an appreciate spread in speed at SoLo’s location (Zaslavsky et al. 2021). Cross-comparing PSP and SoLo impactor distributions for similar populations, particularly if β -meteoroids could be isolated in both, would provide an exciting opportunity to evaluate the evolution of the size distribution as a function of heliocentric distances.

The population of β -meteoroids was specifically excluded from the calculation of mass indices in this study to focus solely on α -meteoroids which should have a smaller spread in impact speed. If the power-law index found here holds down to β -meteoroids, future modeling efforts to understand how a size distribution of β -meteoroids produced very near the Sun could be com-

pared to all existing and future measurements of β -meteoroids from PSP, SoLo, STEREO, WIND, and/or any other spacecraft with the capability to detect β -meteoroids throughout the inner heliosphere (Juhász & Horányi 2013; O’Brien et al. 2018; Poppe & Lee 2020, 2022).

5. DISCUSSION AND CONCLUSIONS

Leveraging PSP’s eccentric orbit, we identify a region near the Sun from 0.1-0.25 au where PSP is effectively only observing bound α -meteoroids due to the very low relative impact speeds and corresponding fluxes from β -meteoroids in this region. From these observations, we derive the cumulative power-law mass index to be $\alpha = 1.1 \pm 0.3$ for grains with radii in the approximate range of ~ 0.6 -1.4 μm . These results quantitatively demonstrate the meteoroid size distribution near the Sun differs substantially from the distribution at 1 au. In contrast to expectations, we find most of the collisional fragments produced in the near-Sun environment inside 0.15 au are overwhelmingly partitioned into sub-micron β -meteoroids, which are effectively “blown out” of the solar system via the Sun’s radiation pressure, or even smaller grains that could become electromagnetically coupled to the solar magnetic field (Czechowski & Mann 2012). The mass index also increases for decreasing heliocentric distance, suggesting even smaller fragments are produced closer to the Sun. The discrepancy between the lower expected mass index and higher value found here could be due to the intense fragmentation process occurring in the very near-Sun environment,

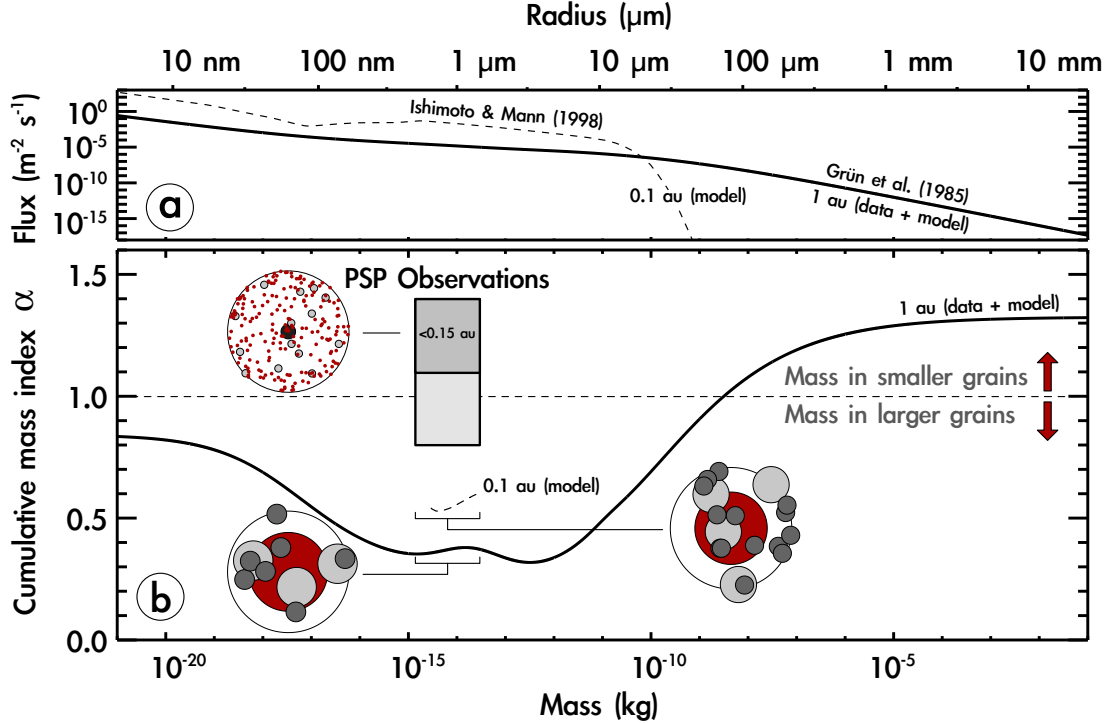


Figure 8. Comparison with size distribution at 1 au (Grün et al. 1985) derived from a large number of observations, as well as the modeled distribution at 0.1 au (Ishimoto & Mann 1998). The grey boxes shows the values of α found here for grains with radii in the approximate range of ~ 0.6 - $1.4 \mu\text{m}$ detectable by PSP.

where impact speeds between grains are likely the highest in the solar system and may provide significantly different fragmentation products compared to lower-speed impacts farther from the Sun. The canonical mass flux at 1 au from Grün et al. (1985) is often scaled by $r^{-0.5}$ to estimate the dust flux at different heliocentric distances; these findings demonstrate that the 1 au fluxes cannot be simply scaled to estimate the near-Sun dust distribution.

For this analysis, we assume collisions are driving the size distribution near the Sun. Furthermore, to interpret the mass indices derived here we assume collisional fragmentation produces only dust grains as fragmentation products and consider the production of impact vapor/plasma negligible compared to the mass of the fragments. While modeling efforts have been investigated on grain destruction and the role of vaporization (e.g. Borkowski & Dwek 1995), we elected not to include more complex origin mechanisms in order to interpret the derived mass-indices with minimal assumptions, which future analyses could explore.

In addition to collisions, sublimation is certainly also operating on grains that transit very near the Sun, where grains are expected to strongly sublimate within $\sim 10 R_{\odot}$ (Mann et al. 2004). However, the location of peak production of β -meteoroids from a collision

model was found to be consistent with the derived β -meteoroid fluxes to PSP, such that collisions were inferred to be the driving phenomenon for dust grain populations observed by PSP (Szalay et al. 2021). Additionally, a comprehensive dynamical meteoroid model which includes fragmentation and the production of β -meteoroids was found to well-match the PSP observations of β -meteoroid fluxes in the inner heliosphere (Pokorný et al. 2024).

Additionally, we assume that transport effects have not significantly modified the collisionally produced size distribution from their sources such that the collisional fragmentation index $\eta = \alpha$. We anticipate most of the collisions occur below 0.1 au (Szalay et al. 2021), such that the small α -meteoroids we measure outside this distance are likely to have been produced at similar radial distances and may not have been significantly evolved from their original source mass distributions. Future efforts could investigate the effects of transport, specifically how the mass-dependent Poynting-Robertson drag would further modify collisional mass distributions.

Rotational disruption due to radiative torque from sunlight on irregular grains has also been proposed to play an important role for dust evolution within our solar system and in astrophysical systems (Miconi 1993; Silsbee & Draine 2016; Hoang et al. 2019). While grains

released from comets have been found to be imparted with rotation due to gas drag (Čapek 2014), the extent to which grains experience radiative torques has not been observationally constrained in the zodiacal cloud. While we cannot assess the extent to which rotational disruption plays a role in the zodiacal dust evolution, the size distribution found here provides constraints for any model that would predict the mass partitioning of rotationally disrupted grains and their relative contribution to the overall zodiacal dust population.

Particles originating from short-period comets have been shown to be resilient to collisions with the zodiacal cloud and have higher fragmentation strength than commonly assumed (Pokorný et al. 2024). This translates to longer collisional lifetimes, the ability of larger particles to migrate closer to the Sun, and a smaller fraction of interplanetary dust particles lost to collisions. The higher particle collisional strength might explain the discrepancy in the value of α between our work and existing models (Grün et al. 1985; Ishimoto & Mann 1998), as shown in Figure 8. More particles are able to migrate into the very inner heliosphere to then be detected by PSP without being collisionally fragmented into nano-dust particles that are not detectable by PSP instruments. Our results might provide a crucial missing piece of evidence for determining the crushing laws in the zodiacal cloud and for models of collisional evolution of interplanetary dust clouds (Pokorný et al. 2024; Poppe 2016; Poppe et al. 2019).

We also note that a fundamental dust grain unit size on the order of 10's of μm was found from observations of cometary dust from 67/C-G, interpreted to be the remnants of the early accretion processes (Hornung et al. 2023). If there are grains that represent more 'fundamental units', they could be more resilient to fragmentation than their aggregates. The Grün et al. (1985) curve in Figure 8 shows a steep decline in the value of α once the particle radius drops below $\sim 100 \mu\text{m}$, perhaps suggestive that grains of this size are more resilient to fragmentation. While Hornung et al. (2023) report their findings using the in-situ experiment on 69P/C-G, the Grün et al. (1985) model is based on spacecraft observations from HEOS2, Pioneers 8 and 9, and from lunar microcraters, all at 1 au. Interplanetary dust particles experience complex space weathering during their lifetime which influences their chemical composition as well as their size-frequency distribution. While the discrepancy is apparent, how grain fragments relate to the original makeup of their parent grains cannot be directly determined from this analysis, yet provides an interesting topic for further investigation.

These results can also be applicable to exozodiacal disks. The grain size distribution, as well as the local stellar conditions at exozodiacal systems, controls the total accretion rate of dust onto exoplanets (Arras et al. 2022). The relative partitioning into α -meteoroids and β -meteoroids in exozodiacal disks plays an important role in their collisional evolution and dictates how remote measurements from these disks are interpreted (Krivov et al. 2000). For example, it was found that β -meteoroid fluxes within the debris disk of β Pictoris could be so large they significantly contribute to the fragmentation of α -meteoroids, hence they may modify the size distribution of their parent α -meteoroids and govern the size dominating in overall cross-section that would be remotely detectable (Krivov et al. 2000). β -meteoroids were also found to play an important role in the luminosities of debris disk halos, where an updated size-frequency distribution could aid in the interpretation of optical and near-IR observations of these halos (Thebault et al. 2023).

Summarizing our results,

- The cumulative mass index for grains with radii of $\sim 0.6\text{--}1.4 \mu\text{m}$ (masses of 3×10^{-15} to 3×10^{-14} kg) is found to be $\alpha = 1.1 \pm 0.3$ from $0.1\text{--}0.25 R_{\odot}$
- The cumulative mass index increases toward the Sun, with even smaller collisional fragments generated closer to the Sun.
- The derived size distribution is steeper than previously estimated, and in contrast to expectations we find most of the dust mass resides in the smallest fragments inside 0.15 au and not in large grains.
- These results place new constraints how the solar system's zodiacal cloud and by extension astrophysical debris disks are partitioned in mass.

In conclusion, PSP observations provide a unique platform to observe the inner-most regions of our zodiacal dust disk. While PSP does not have a dedicated dust instrument, impacts detected by its electric field instrument can be used to quantitatively constrain the multiple populations in the near-Sun dust environment. These observations are taken in the nearest region to the Sun ever explored in-situ by spacecraft and provide a critical window into the complex evolution of our zodiacal cloud.

Acknowledgements. We thank the many Parker Solar Probe team members that enabled these observations. We thank B. Draine, M. Horanyi, B. Hensley, & K. Silsbee for helpful discussions on grain fragmentation,

D. McComas & G. Livadiotis for helpful discussions related to the power-law analyses, and D. P. Morgan & S. P. Childress for graphical guidance. We also thank the two anonymous reviewers for their helpful comments during review. We acknowledge NASA Parker Solar Probe Guest Investigator grant 80NSSC21K1764. P.P. was additionally supported by NASA Solar System

Workings award number 80NSSC21K0153, a cooperative agreement 80GSFC21M0002, and NASA’s Planetary Science Division Research Program, through ISFM work packages EIMM and Planetary Geodesy at NASA Goddard Space Flight Center. We used the “managua” & “bukavu” colormaps (Crameri et al. 2020) for Figures 3 & 4.

APPENDIX

A. CONSTRAINING THE UNCERTAINTY IN ESTIMATING THE MASS INDEX

When a high-speed dust grain with mass m_{imp} and speed v_{imp} impacts a surface (PSP) it produces an impact charge $Q_{\text{imp}} \propto m_{\text{imp}}^a v_{\text{imp}}^b$, where the exponents a , b and proportionality constant are determined empirically based on the surface properties (Auer 2001). Typical spacecraft surface materials have a mass exponent of 1 (Collette et al. 2014), and we adopt this value here. . For the speed dependence, we assume the impact speed has a functional form of $v_{\text{imp}} = \bar{v}_{\text{imp}} m_{\text{imp}}^c$, such that there is a separable component of the impact speed that depends on mass and \bar{v}_{imp} has no mass dependence. Combining the empirically determined mass exponent with a value of 1.0 with the additional mass dependence from the impact speed, the mass dependent exponent of the impact charge is $a = 1 + \delta a$, where $\delta a = bc$

The velocity index b has been empirically determined for a variety of spacecraft materials. MLI (multi-layer thermal insulation) covers much of the spacecraft and is the most likely target material to be hit by dust and produce impact signals for bound grains post perihelion that would impact the spacecraft body instead of the heat shield (Szalay et al. 2020). We therefore assuming an exponent of $b = 4.7$ for MLI (Collette et al. 2014).

With such a relation between Q and m , the cumulative charge index is given by $\alpha_Q = \alpha/a = \alpha/(1 + \delta a)$. Therefore, the cumulative mass index is related to the

cumulative impact charge index by

$$\alpha = \alpha_Q(1 + \delta a) \quad (\text{A1})$$

To calculate the mass-dependent component of the impact speed, δa , we investigate the dependence of the dust impact speed to PSP. For motion in a two-dimensional orbital plane, a body in a bound orbit about the Sun has an orbital velocity such that

$$\begin{aligned} v &= \sqrt{\mu(1 - \beta) \left(\frac{2}{r} - \frac{1}{a} \right)} \\ v_\varphi &= \frac{\sqrt{\mu(1 - \beta)a(1 - e^2)}}{r} \\ v_r &= \pm \sqrt{\mu(1 - \beta) \left(\frac{2}{r} - \frac{1}{a} - \frac{a(1 - e^2)}{r^2} \right)} \end{aligned}$$

where $\mu = GM_\odot = 1.327 \times 10^{20} \text{ m}^3 \text{ s}^{-2}$ is the standard solar gravitational parameter, β is the mass-dependent ratio of the radiation pressure and gravitational forces from the Sun (Zook & Berg 1975; Burns et al. 1979; Wilck & Mann 1996), r is the heliocentric distance, e is the eccentricity, and a is the semi-major axis. These equations also apply to PSP with $\beta = 0$.

To reduce complexity in the following calculation, we assume each impacting grain is on a Keplerian orbit with a semi-major axis equal to the heliocentric distance of PSP at any location, such that $a_d = r$, and that grains are in the same orbital plane as PSP. With these assumptions, the dust impact speed $v_{\text{imp}} = |\vec{v}_d - \vec{v}_{\text{PSP}}|$ to PSP is

$$v_{\text{imp}} = \sqrt{\mu \left[\frac{2}{r} - \frac{1}{a} + \frac{1 - \beta}{r} - 2\sqrt{\frac{(1 - \beta)a(1 - e^2)(1 - e_d^2)}{r^3}} \pm 2e_d \sqrt{\frac{(1 - \beta)}{r} \left(\frac{2}{r} - \frac{1}{a} - \frac{a(1 - e^2)}{r^2} \right)} \right]} \quad (\text{A2})$$

where the mass dependence is from $\beta(m)$, e_d is the eccentricity of the dust, $a = 0.41 \text{ au}$ & $e = 0.85$ are the semi-major axis and eccentricity of PSP during orbits

10-16. The \pm has a positive value when PSP and the dust grain have the opposite sign for their radial velocity components (e.g. post-perihelion outbound PSP

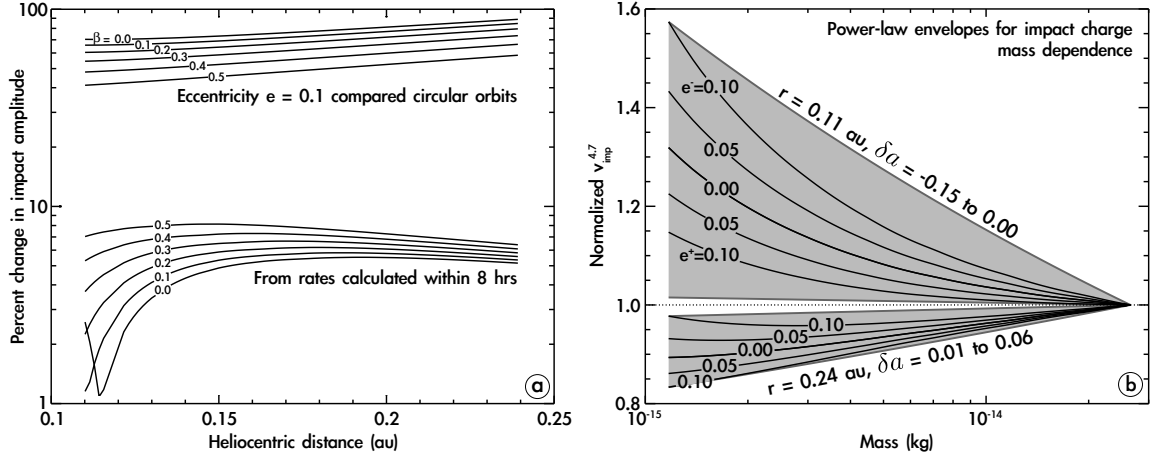


Figure 9. (a) Percent change in the impact amplitude due to the finite cadence of 8 hr impact rate intervals and due to the possible eccentricity of the grains. For each effect, six curves are shown corresponding to $\beta = 0 - 0.5$. (b) Power-law envelopes to the family of normalized mass-dependent impact charge curves for heliocentric distances of 0.11 au and 0.24 au.

and inbound dust grains), and negative when the radial velocity components have the same sign. This impact speed relation will allow us to constrain the uncertainties of our estimates for α discussed at the end of this section.

With the analytic expression for the impact speed to PSP given in Eq. A2 we can estimate the uncertainty in determining the mass index due to three effects that all vary as a function of heliocentric distance. First, all impact rates are calculated in 8-hour intervals, which introduces a small uncertainty on the impact speeds. Figure 9a shows the percent change in impact charge amplitude calculated via $(1 + \Delta v/v)^{4.7}$ due to this effect, where v is the impact speed to PSP from a grain on a circular, Keplerian orbit in the center of an 8-hr interval for each distance and Δv is the maximum expected difference between v and the impact speeds within the entire 8-hr interval. For the region investigated, this introduces an impact amplitude uncertainty of $<10\%$ and therefore we neglect this effect.

The next effect we investigate is possible uncertainty in impact speed due to grains having a non-zero eccentricity. Zodiacal grains very near the Sun are expected to have low eccentricities due to circularization from Poynting-Robertson drag and we consider the case for grains that have eccentricities of up to 0.1 (Pokorný et al. 2024). Figure 9a shows the percent change in impact charge amplitude due to such non-circular impactors and we find this introduces an uncertainty in the impact charge amplitude of up to a factor of 2 which translates to a factor of $\sqrt[3]{2} \approx 1.3$ in radius. As grains on circular orbits would have the slowest impact speed compared to eccentric grains with the same other orbital

parameters, this uncertainty means we may be overestimating the impactor grain size by a factor of ~ 1.3 .

Both of these uncertainties do not introduce any mass-dependent bias and therefore would not affect the determination of the mass index, they would only affect the estimate of the relevant size range to which the mass index is valid. The third source of uncertainty we consider is due to the impact speed having a mass dependence, which does introduce a mass-dependent bias and propagates to our estimates of $\alpha = \alpha_Q(1 + \delta a)$.

To quantify δa , we calculate the impact speed to PSP given in Eq. A2 as a function of mass, where the mass dependence is solely from $\beta(m)$. We use the $\beta(m)$ relation corresponding to “old cometary” grains according to Wilck & Mann (1996). For the size range considered, β has values near 0.5 on the lowest mass end and 0.2 on the upper mass end. Figure 9b shows two sets of normalized $v_{\text{imp}}^{4.7}$ curves corresponding to the heliocentric distance boundaries of 0.11 au and 0.24 au considered here. Multiple curves for each family are shown for different values of eccentricity between 0 and 0.1 and using the + or − sign in Eq. A2, with the curves corresponding to a minus sign as the top two of each family and those corresponding to a plus sign as the bottom two. We then determine the slope of power-laws that provide an envelope to these family of curves for each heliocentric distance. In the examples given in Figure 9b, we find power-law functional forms with $\delta a = -0.15$ to 0 provide an envelope for the family of curves corresponding to $r = 0.11$ au and $\delta a = 0.01$ to 0.06 for $r = 0.24$ au. We calculate these envelopes over the entire range of heliocentric distances considered in this study to determine the range of δa minimum and maximum values.

REFERENCES

- Andersson, L., Weber, T. D., Malaspina, D. M., et al. 2015, *Science*, 350, 0398
- Arras, P., Wilson, M., Pryal, M., & Baker, J. 2022, *The Astrophysical Journal*, 932, 90
- Auer, S. 2001, in *Interplanetary Dust*, ed. E. Grün, B. Gustafson, S. Dermott, & H. Fechtig. (Springer), 387–438
- Bale, S. D., Goetz, K., Harvey, P. R., et al. 2016, *Space Science Reviews*, 204, 49
- Borkowski, K. J., & Dwek, E. 1995, *ApJ*, 454, 254, doi: [10.1086/176480](https://doi.org/10.1086/176480)
- Burns, J. A., Lamy, P. L., & Soter, S. 1979, *Icarus*, 40, 1, doi: [10.1016/0019-1035\(79\)90050-2](https://doi.org/10.1016/0019-1035(79)90050-2)
- Collette, A., Grün, E., Malaspina, D. M., & Sternovsky, Z. 2014, *Journal of Geophysical Research-Space Physics*, 119, 6019
- Collette, A., Sternovsky, Z., & Horányi, M. 2014, *Icarus*, 227, 89, doi: [10.1016/j.icarus.2013.09.009](https://doi.org/10.1016/j.icarus.2013.09.009)
- Crameri, F., Shephard, G. E., & Heron, P. J. 2020, *Nature Communications*, 11, 5444, doi: [10.1038/s41467-020-19160-7](https://doi.org/10.1038/s41467-020-19160-7)
- Cukier, W. Z., & Szalay, J. R. 2023, *The Planetary Science Journal*, 4, 109, doi: [10.3847/psj/acd538](https://doi.org/10.3847/psj/acd538)
- Czechowski, A., & Mann, I. 2012, *Nanodust in the Solar System: Discoveries and Interpretation* (Springer, Astrophysics and Space Science Library 385)
- Dohnanyi, J. 1969, *Journal of Geophysical Research*, 74, 2531
- Fox, N., Velli, M. C., Bale, S. D., et al. 2016, *Space Science Reviews*, 204, 7
- Gault, D. E., & Wedekind, J. A. 1969, *Journal of Geophysical Research*, 74, 6780
- Grün, E., Pailer, N., FECHTIG, H., & Kissel, J. 1980, *Planetary and Space Science*, 28, 333
- Grün, E., Zook, H. A., Fechtig, H., & Giese, R. H. 1985, *Icarus*, 62, 244, doi: [10.1016/0019-1035\(85\)90121-6](https://doi.org/10.1016/0019-1035(85)90121-6)
- Gurnett, D. A., Grun, E., Gallagher, D., Kurth, W. S., & Scarf, F. L. 1983, *Icarus*, 53, 236, doi: [10.1016/0019-1035\(83\)90145-8](https://doi.org/10.1016/0019-1035(83)90145-8)
- Hoang, T., Tram, L. N., Lee, H., & Ahn, S.-H. 2019, *Nature Astronomy*, 3, 766, doi: [10.1038/s41550-019-0763-6](https://doi.org/10.1038/s41550-019-0763-6)
- Horányi, M., Szalay, J. R., Kempf, S., et al. 2015, *Nature*, 522, doi: [10.1038/nature14479](https://doi.org/10.1038/nature14479)
- Hornung, K., Mellado, E. M., Stenzel, O. J., et al. 2023, *Planetary and Space Science*, 236, 105747, doi: [10.1016/j.pss.2023.105747](https://doi.org/10.1016/j.pss.2023.105747)
- Ishimoto, H., & Mann, I. 1998, *Planetary and Space Science*, 47, 225
- Juhász, A., & Horányi, M. 2013, *Geophys. Res. Lett.*, 40, 2500, doi: [10.1002/grl.50535](https://doi.org/10.1002/grl.50535)
- Kellogg, P. J., Goetz, K., & Monson, S. J. 2016, *Journal of Geophysical Research-Space Physics*, 121, 966
- Krivov, A. V., Mann, I., & Krivova, N. A. 2000, *Astronomy and Astrophysics*, 362, 1127
- Laakso, H., Grard, R., Pedersen, A., & Schwehm, G. 1989, *Advances in Space Research*, 9, 269, doi: [10.1016/0273-1177\(89\)90273-1](https://doi.org/10.1016/0273-1177(89)90273-1)
- Malaspina, D. M., Horanyi, M., Zaslavsky, A., et al. 2014, *Geophysical Research Letters*, 41, 266
- Malaspina, D. M., O'Brien, L. E., Thayer, F., Sternovsky, Z., & Collette, A. 2015, *Journal of Geophysical Research-Space Physics*, 120, 6085
- Malaspina, D. M., Toma, A., Szalay, J. R., et al. 2023, *The Astrophysical Journal Supplement Series*, 266, 21, doi: [10.3847/1538-4365/acca75](https://doi.org/10.3847/1538-4365/acca75)
- Malaspina, D. M., Ergun, R. E., Bolton, M., et al. 2016, *Journal of Geophysical Research-Space Physics*, 121, 5088
- Malaspina, D. M., Szalay, J. R., Pokorný, P., et al. 2020, *Observations of Inner Heliospheric Dust Variability*
- Mann, I., & Czechowski, A. 2020, *Astronomy and Astrophysics*, 1
- Mann, I., Kimura, H., Biesecker, D. A., et al. 2004, *Space Science Reviews*, 110, 269
- Misconi, N. Y. 1993, *Journal of Geophysical Research: Space Physics*, 98, 18951, doi: [10.1029/93ja01521](https://doi.org/10.1029/93ja01521)
- O'Brien, L., Juhász, A., Sternovsky, Z., & Horányi, M. 2018, *Planetary and Space Science*, 156, 7, doi: <https://doi.org/10.1016/j.pss.2017.11.013>
- Page, B., Bale, S. D., Bonnell, J. W., et al. 2020, *Examining Dust Directionality with the Parker Solar Probe FIELDS Instrument*
- Piquette, M., Poppe, A., Bernardoni, E., et al. 2019, *Icarus*, 321, 116, doi: [10.1016/j.icarus.2018.11.012](https://doi.org/10.1016/j.icarus.2018.11.012)
- Pokorný, P., & Brown, P. G. 2016, *Astronomy & Astrophysics*, 592, A150, doi: [10.1051/0004-6361/201628134](https://doi.org/10.1051/0004-6361/201628134)
- Pokorný, P., Moorhead, A. V., Kuchner, M. J., Szalay, J. R., & Malaspina, D. M. 2024, *The Planetary Science Journal*, 5, 82, doi: [10.3847/PSJ/ad2de8](https://doi.org/10.3847/PSJ/ad2de8)
- Poppe, A., & Lee, C. 2020, *Journal of Geophysical Research: Space Physics*, 125, e2020JA028463
- . 2022, *Journal of Geophysical Research: Space Physics*, 127, e2022JA030317
- Poppe, A. R. 2016, *Icarus*, 264, 369
- Poppe, A. R., Lisse, C. M., Piquette, M., et al. 2019, *The Astrophysical Journal Letters*, 881, 0, doi: [10.3847/2041-8213/ab322a](https://doi.org/10.3847/2041-8213/ab322a)

- Pusack, A., Malaspina, D. M., Szalay, J. R., et al. 2021, PSJ
- Shen, M. M., Sternovsky, Z., & Malaspina, D. M. 2023, Journal of Geophysical Research: Space Physics, 128, doi: [10.1029/2022ja030981](https://doi.org/10.1029/2022ja030981)
- Silsbee, K., & Draine, B. T. 2016, The Astrophysical Journal, 818, 133, doi: [10.3847/0004-637x/818/2/133](https://doi.org/10.3847/0004-637x/818/2/133)
- Sommer, M. 2023, Planetary and Space Science, 236, 105751, doi: [10.1016/j.pss.2023.105751](https://doi.org/10.1016/j.pss.2023.105751)
- Stenborg, G., Howard, R., Hess, P., & Gallagher, B. 2020, Astronomy and Astrophysics, doi: [10.1051/0004-6361/202039284](https://doi.org/10.1051/0004-6361/202039284)
- Sterken, V. J., Altobelli, N., Kempf, S., et al. 2012, A&A, 538, A102, doi: [10.1051/0004-6361/201117119](https://doi.org/10.1051/0004-6361/201117119)
- Strub, P., Sterken, V. J., Soja, R., et al. 2019, Astronomy and Astrophysics, 621, A54
- Szalay, J. R., Pokorný, P., Bale, S. D., et al. 2020, The Astrophysical Journal Supplement Series, 246, 27, doi: [10.3847/1538-4365/ab50c1](https://doi.org/10.3847/1538-4365/ab50c1)
- Szalay, J. R., Pokorný, P., Malaspina, D. M., et al. 2021, The Planetary Science Journal, 2, 185, doi: [10.3847/psj/abf928](https://doi.org/10.3847/psj/abf928)
- Thebault, P., Olofsson, J., & Kral, Q. 2023, A&A, 674, A51, doi: [10.1051/0004-6361/202345995](https://doi.org/10.1051/0004-6361/202345995)
- Tsurutani, B. T., Clay, D. R., Zhang, L. D., et al. 2003, Geophysical Research Letters, 30, 2134
- Tsurutani, B. T., Clay, D. R., Zhang, L. D., et al. 2004, Icarus, 167, 89, doi: [10.1016/j.icarus.2003.08.021](https://doi.org/10.1016/j.icarus.2003.08.021)
- Vaverka, J., Pavlů, J., Nouzák, L., et al. 2019, Journal of Geophysical Research-Space Physics, 124, 8179
- Vaverka, J., Nakamura, T., Kero, J., et al. 2018, Journal of Geophysical Research-Space Physics, 123, 6119
- Wehry, A., & Mann, I. 1999, A&A, 341, 296
- Wilck, M., & Mann, I. 1996, Planetary and Space Science, 44, 493
- Ye, S.-Y., Gurnett, D. A., Kurth, W. S., et al. 2014, Journal of Geophysical Research: Space Physics, 119, 6294, doi: <https://doi.org/10.1002/2014JA020024>
- Zaslavsky, A., Meyer-Vernet, N., Mann, I., et al. 2012, Journal of Geophysical Research (Space Physics), 117, 5102, doi: [10.1029/2011JA017480](https://doi.org/10.1029/2011JA017480)
- Zaslavsky, A., Mann, I., Soucek, J., et al. 2021, Astronomy & Astrophysics, 656, A30, doi: [10.1051/0004-6361/202140969](https://doi.org/10.1051/0004-6361/202140969)
- Zook, H. A., & Berg, O. E. 1975, Planetary and Space Science, 23, 183 , doi: [https://doi.org/10.1016/0032-0633\(75\)90078-1](https://doi.org/10.1016/0032-0633(75)90078-1)
- Čapek, D. 2014, Astronomy & Astrophysics, 568, A39, doi: [10.1051/0004-6361/201423857](https://doi.org/10.1051/0004-6361/201423857)